MDPI

Article

Ice Coverage Induced by Depositing a Water Drop onto the Supercooled Substrate at Extreme Low Vapor Pressure

Yugang Zhao [1,2,*], Zichao Zuo [1], Haibo Tang [1] and Xin Zhang [3]

1 Shanghai Key Laboratory of Multiphase Flow and Heat Transfer in Power Engineering, School of Energy and Power Engineering, University of Shanghai for Science and Technology, Shanghai 200093, China; 202390111@st.usst.edu.cn (Z.Z.); 202390081@st.usst.edu.cn (H.T.)
2 Key Laboratory of Icing and Anti/De-Icing, China Aerodynamics Research and Development Center, Mianyang 621000, China
3 State Key Laboratory of Aerodynamics, China Aerodynamics Research and Development Center, Mianyang 621000, China; lookzx@mail.ustc.edu.cn
* Correspondence: ygzhao@usst.edu.cn

Abstract: Icing/snowing/frosting is ubiquitous in nature and industrial processes, and the accretion of ice mostly leads to catastrophic consequences. The existing understanding of icing is still limited, particularly for aircraft icing, where direct observation of the freezing dynamics is inaccessible. In this work, we investigate experimentally the impact and freezing of a water drop onto the supercooled substrate at extremely low vapor pressure, to mimic an aircraft passing through clouds at a relatively high altitude, engendering icing upon collisions with pendant drops. Special attention is focused on the ice coverage induced by an impinging drop, from the perimeter pointing outward along the radial direction. We observed two freezing regimes: (I) spread-recoil-freeze at the substrate temperature of $T_s = -15.4 \pm 0.2\,^\circ\text{C}$ and (II) spread (incomplete)-freeze at the substrate temperature of $T_s = -22.1 \pm 0.2\,^\circ\text{C}$. The ice coverage is approximately one order of magnitude larger than the frozen drop itself, and counterintuitively, larger supercooling yields smaller ice coverage in the range of interest. We attribute the variation of ice coverage to the kinetics of vapor diffusion in the two regimes. This fundamental understanding benefits the design of new anti-icing technologies for aircraft.

Keywords: aircraft icing; anti-icing; drop impinging; ice coverage

1. Introduction

Icing, in the forms of bulk ice, snow, frost and others, is a fascinating phenomenon that occurs widely in nature [1–4]. However, icing in many industries is unwanted, leading to detrimental and occasionally catastrophic consequences [5,6]. In HVAC&R (heating, ventilating, air conditioning and refrigerating) systems, heat exchangers that operate in supercooled and humid environments are inevitably covered with a thick layer of frost, yielding a non-negligible thermal resistance [7–9]. Therefore, both the system integrity and the coefficient of performance are affected drastically. Despite being a complex and unorthodox phase change problem, an appreciable portion of the physics underlying condensation frosting has been revealed recently as an in situ observation of frosting dynamics and is accessible in most experiments [10–12]. Abundant anti-/de-frosting technologies [13–18], both passive and active, have been developed to mitigate frosting problems.

Existing studies on another very important type of icing, aircraft icing [19,20], are relatively limited, owing to the simple fact that direct observation of the freezing dynamics is inaccessible for aircraft icing. In the literature [21–26], some researchers use impinging drops on a supercooled substrate to mimic the scene in which icing occurs upon collisions of pendant drops when an aircraft passes through clouds at a relatively high altitude. The effects of surface chemistry and topography [27–30], drop size and impinging velocity

in terms of Weber number [31,32], and system alignments [33–38] have been studied extensively to reveal the freezing mechanism and evaluate the anti-icing performance of each proposed anti-/de-icing method. Whereas these studies only focus on the spreading and freezing of impinging drops themselves, little attention is paid to the transport and phase change of the accompanying water vapor, which originates from the liquid-gas interface of the impinging drops and diffuses to the surroundings under a concentration gradient [39,40]. Once this vapor condenses and becomes frozen around a main impinging drop, the actual ice coverage can be much larger than that covered directly by the frozen drop itself. Note that ice grows thicker rapidly on all the covered regions as a result of a massive supply of water vapor once the aircraft starts to descend.

In this work, we study the dynamics of a pendant water drop impinging and freezing on the supercooled substrate at an extremely low vapor pressure, with special attention to the vapor transport and the resultant extra ice coverage. We observe two freezing regimes at different degrees of supercooling: (I) spread-recoil-freeze at a higher substrate temperature of $T_s = -15.4 \pm 0.2$ °C and (II) spread (incomplete)-freeze at a lower substrate temperature of $T_s = -22.1 \pm 0.2$ °C. Unlike what has been reported in the literature, we find a thin layer of condensate/frost forms, surrounding the main drop and covering a region of the size of one order of magnitude larger than that directly covered by the frozen drop itself. Counterintuitively, larger supercooling yields smaller ice coverage in the range of interest. We attribute the variation in ice coverage to the kinetics of vapor diffusion in the two regimes. The competition of three characteristic time scales, i.e., the spreading time, the icing nucleation time, and the cooling time, determines the impact and freezing behaviors of the impinging drop, which in turn determines the intensity and lifespan of vapor emission and thus the size of ice coverage.

2. Materials and Methods

2.1. Substrate Treatment and Characterization

We prepared a smooth hydrophobic silicon substrate to carry the freezing drops. A single-side polished single crystal silicon water was chosen as the base material, as its atomic smoothness can minimize the effect of surface heterogeneity. First, a raw silicon wafer was cut into squares of 4×4 cm^2. Second, the substrate was cleaned following a standard protocol [41,42], i.e., rinsing subsequently with acetone, isopropyl alcohol and deionized water, and dried in a nitrogen gas flow. Third, the substrate was silanized by a two-step process consisting of a 30 min oxygen plasma treatment (SmartPlasma 2, Plasma technology, Herrenberg, Germany) and a chemical vapor deposition (CVD) of trichloro (1H, 1H, 2H, 2H-perfluorooctyl) silane (Sigma-Aldrich, Saint Louis, MO, USA). Once removed from the CVD chamber, the substrate becomes hydrophobic as its surface is bonded with a monolayer of silane molecules. Right before every experiment, the substrate was cleaned again by rinsing with isopropyl alcohol and deionized water and dried in a nitrogen gas flow. The wettability of the prepared substrate was characterized by measuring the static contact angle of a 5 μL deionized water drop using a high-resolution goniometer (FTA200, Attension Theta, Västra Frölunda, Sweden). Results from the measurement show that the static contact angle was $43.5 \pm 2°$ and $102 \pm 2°$ for a raw untreated substrate and a silanized substrate, respectively.

2.2. Experimental Setup

We built a customized cryostage to investigate the impact and freezing of a water drop in this work. The liquid used was deionized water (18 MΩ-cm, Millipore, Hatters Ln, Watford, UK). Before the experiments, a container carrying the liquid was put into a vacuum chamber for over 10 min to remove dissolved gas. Figure 1 shows a schematic of the experimental setup. To eliminate the contamination from ambient particles and vapor, the impact and freezing of drops occurred in an enclosure filled with non-condensable gas (nitrogen), with the in-chamber temperature and pressure well balanced with the surroundings of near 1 atmospheric pressure and room temperature $T_\infty = 20.2 \pm 0.5$ °C.

The in-chamber relative humidity was smaller than 2% during the following experiments. The cryostage consisted of a heat sink and a Peltier element, with the former connected to a cooling circulator and the performance of the latter modulated by a Proportional-Integral-Derivative (PID) controller. The prepared substrate was mounted onto the cryostage by applying a thin layer of thermal paste to minimize the contact thermal resistance. During the experiments, a water drop induced by a syringe pump left gently from a quartz capillary tip and impacted the substrate, driven by the gravitational force. Determined by the size of the quartz capillary, each drop generated was of a fixed volume of 7.1 ± 0.2 μL. To avoid splashing where the mother drop broke into multiple small drops, we chose a relatively small deposition height of 30.0 ± 0.1 mm, corresponding to a *We* ~15, where $We = \rho g h d / \sigma$, with ρ being the density of water, g being the gravitational acceleration, h being the deposition height, d being the drop diameter (before impact), and σ being the surface tension of water to air. A high-speed camera was used to capture the freezing dynamics of the impinging drop and the formation of condensation/frosting halo around the mother drop from the top view.
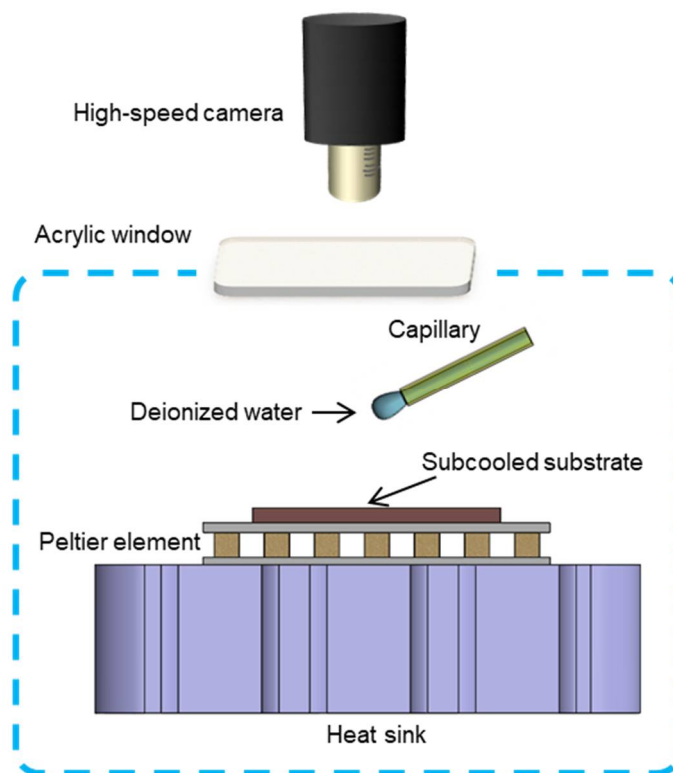

Figure 1. Schematic of the experimental setup.

3. Results and Discussion

We investigated the freezing dynamics of an impinging water drop and the ice coverage induced by its own vapor in extremely low vapor pressure. For the sake of simplicity, we use the term "mother" drop to denote the impinging drop. When the substrate temperature is not sufficiently low at $T_s = -15.4 \pm 0.2$ °C, the mother drop gently impacts the substrate and is stabilized after going through a typical spread-recoil process [43], i.e., regime I. As highlighted in Figure 2, icing nucleation is triggered at t = 150 ms, and the icing front propagates from the substrate base upwards. Freezing of the mother drop is completed at approximately t = 3.9 s. We noticed two characteristic features: (1) a bright halo appears adjacent to the mother drop even before the occurrence of icing nucleation [39] and (2) a small clear gap is located between the halo and the mother drop. Note that the substrate region far beyond the mother drop becomes whiter during the impinging and

freezing of the mother drop, indicating this area is covered with a thin layer of condensate or frost. However, no further reliable information can be extracted from the direct captures.
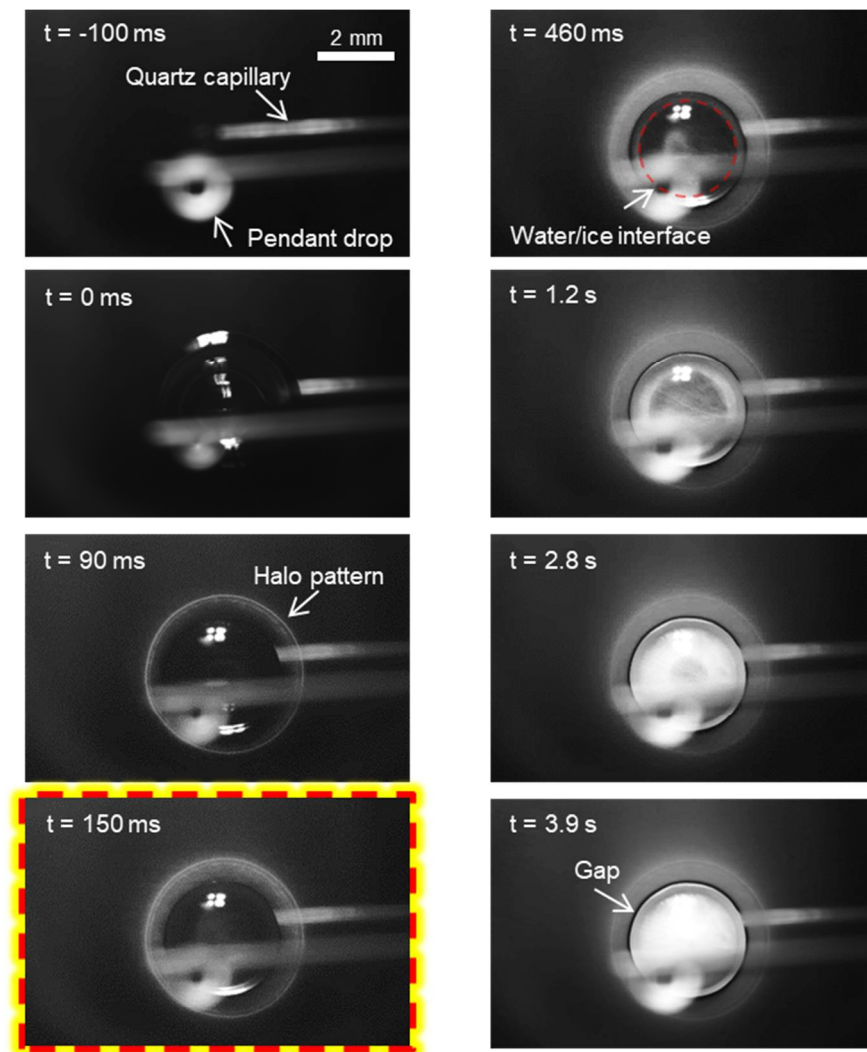
Figure 2. Freezing dynamics of the impinging drop at the substrate temperature of $T_s = -15.4 \pm 0.2\ °C$, i.e., regime I: spread-recoil-freeze. The highlighted capture denotes the onset of icing nucleation.

When the substrate temperature is sufficiently low at $T_s = -22.1 \pm 0.2\ °C$, spreading of the mother drop is interrupted, as shown in Figure 3, i.e., regime II. Icing nucleation occurs almost upon contact between liquid and substrate, at a barely measurable time of t = 3 ms, as highlighted. Spreading of the mother drop is confined in the solidified contact line, and thus the resultant drop shape falls between the maximum spreading and its equilibrium shape when in the liquid state. Owing to an apparently larger contact area and also a lower substrate temperature, the mother drop is frozen in less than 1 s, much faster than that of regime I. In addition, the frozen mother drop is much more clear than that of regime I, particularly near the contact line where the ice crystal is almost transparent (darker). Importantly, the substrate region near the mother drop becomes only slightly brighter after the impinging and freezing of the mother drop, much less pronounced than that in regime I.
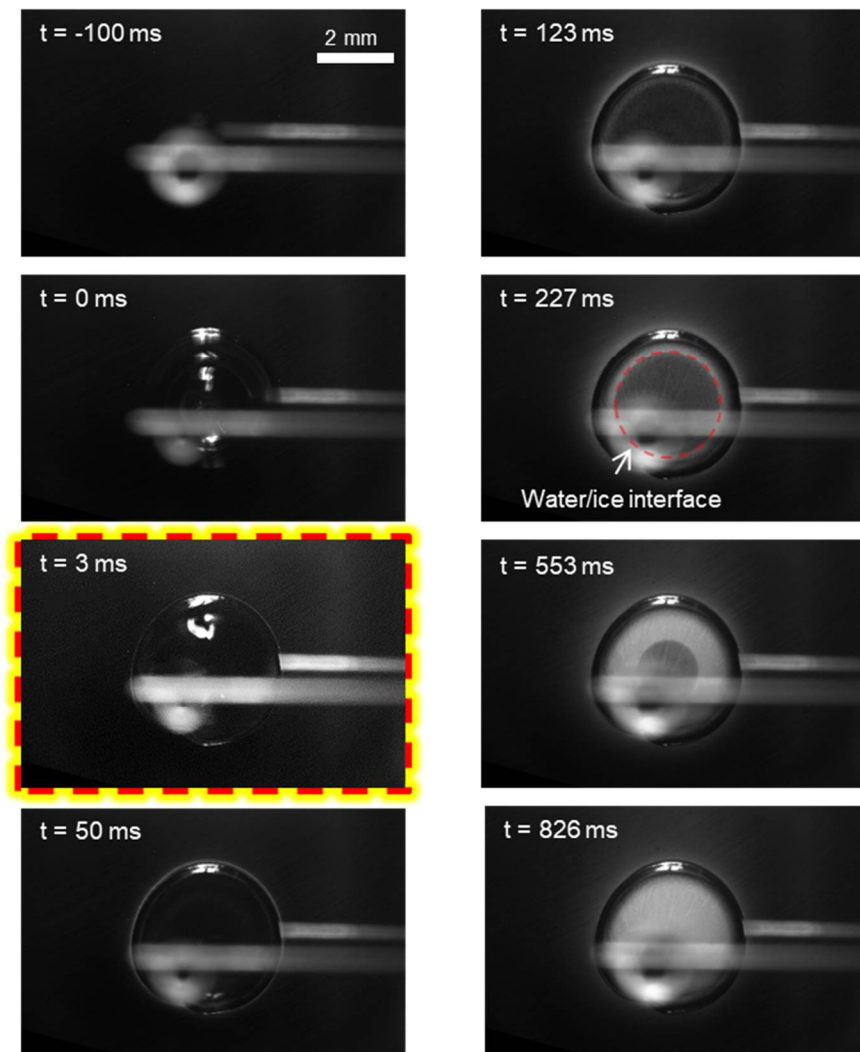
Figure 3. Freezing dynamics of the impinging drop at the substrate temperature of $T_s = -22.1 \pm 0.2\ °C$, i.e., regime II: spread (incomplete)-freeze. The highlighted capture denotes the onset of icing nucleation.

By comparing the direct captures of the two regimes, we can anticipate that an appreciable area of the substrate is covered by the condensate/frost induced by the impinging and freezing of the mother drop. However, we can't detect the edge of this condensate/frost covered area based on the direct captures, i.e., the actual size of ice coverage. Therefore, we propose a Matlab-based image processing program, as shown in Figure 4, to extract the information of this condensate/frost layer. Figure 4a shows the last capture from Figure 2 (regime I) for demonstration. In step 1, we carried out an image calculation by subtracting the background, i.e., the capture right before the incidence of impinging of the mother drop. Figure 4b shows the calculated result, showing only the mother drop and its induced condensate/frost layer. In step 2, we adjusted the local intensity by enhancing the contrast and brightness. Figure 4c shows the final image processing result, from which we can readily identify the edge of the condensate/frost layer. To measure quantitatively the size of ice coverage, we plotted the normalized intensity as a function of the location along the radial direction, as shown in Figure 4d. Note that the contact radius r_c of the mother drop is used as a reference, to indicate the size of actual ice coverage compared to the size of the frozen mother drop itself. The whole substrate is categorized into four sections (for regime I): the frozen mother drop, the depletion zone, the invasion of condensate/frost, and the clear region that is unaffected.
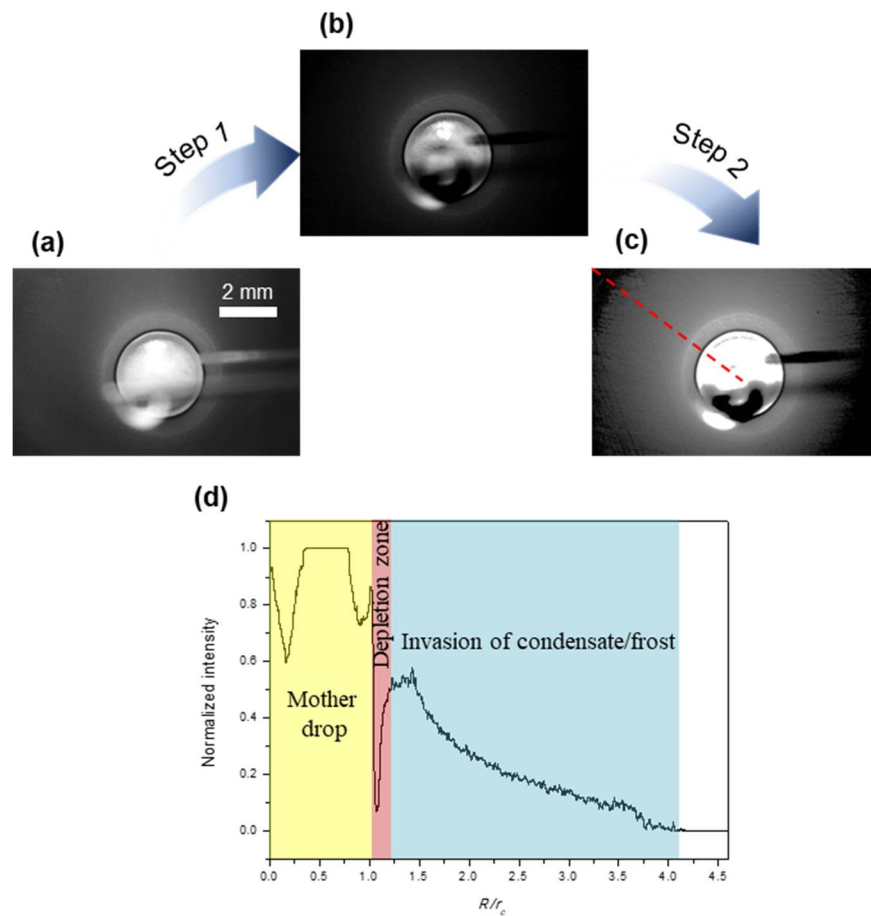
Figure 4. An example showing the imaging processing method (**a**–**c**) and the variation of normalized intensity along the radial direction (**d**).

Figures 5 and 6 show the growing dynamics of the condensate/frost layer during the impact and freezing of the mother drop. For regime I, at the higher substrate temperature of $T_s = -15.4 \pm 0.2$ °C, the condensate/frost layer expands radially from the contact line. The actual ice coverage grows to approximately four times the contact radius of the mother drop, or 16 times the contact area covered by the frozen mother drop. The depletion zone appears after the occurrence of icing nucleation in the mother drop, and its size also increases slightly as the freezing proceeds. For regime II, at the lower substrate temperature of $T_s = -22.1 \pm 0.2$ °C, the condensate/frost layer also expands radially from the contact line after the impinging and freezing of the mother drop. However, the expansion stops at a very early stage of t = 90 ms, and the resultant ice coverage remains constant, whereas the condensate/frost layer only grows thicker afterward. The final ice coverage is only approximately 1.75 times the contact radius of the frozen mother drop, or three times the contact area covered by the frozen mother drop. Note that this result is quite counterintuitive, with a lower substrate temperature yielding a much smaller ice coverage.
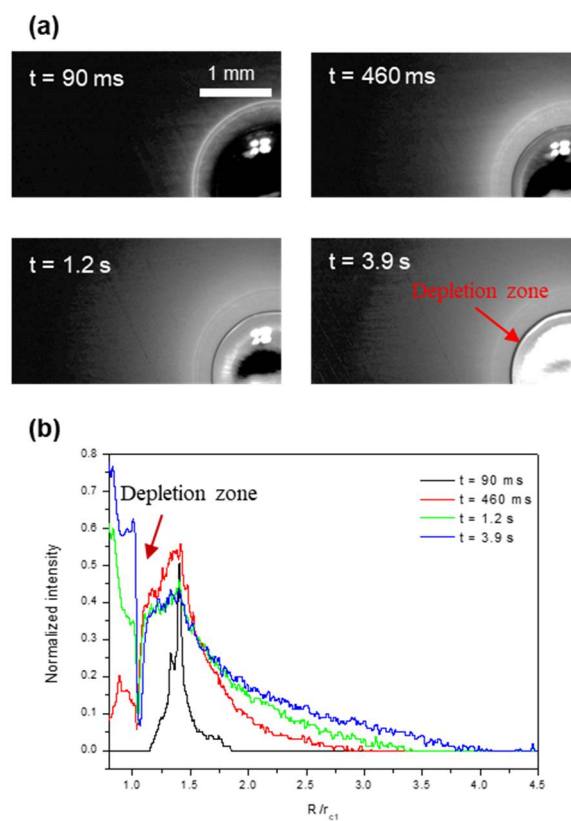
Figure 5. Growing dynamics of the condensate/frost region (**a**) and the resultant intensity profiles (**b**) at the substrate temperature of $T_s = -15.4 \pm 0.2\ °C$.
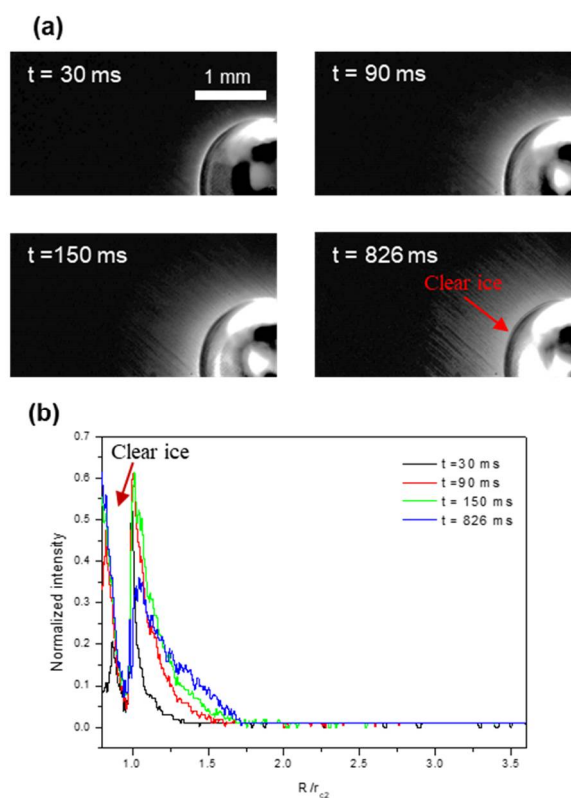

Figure 6. Growing dynamics of condensate/frost region (**a**) and the resultant intensity profiles (**b**) at the substrate temperature of $T_s = -22.1 \pm 0.2\ °C$.

By analyzing the experimental results above, we show that the ice coverage induced by an impinging drop is much larger than the area covered directly by the frozen drop itself. In particular, a higher substrate temperature (regime I) yields a condensate/frost layer of the area of over one order of magnitude of that of the frozen drop. As this condensate/frost layer consists of microdrops from the vapor emitted from the main drop, we need to study the vapor transport kinetics to reveal the physics involved. For a pendant mother drop at room temperature T_∞, it is surrounded by its own vapor due to diffusion-controlled evaporation. This vapor becomes oversaturated once the mother drop approaches the supercooled substrate. Afterward, dynamic behaviors of the mother drop at the two different regimes facilitate or hinder the vapor transfer as determined by the local thermophysical conditions. To explain how the dynamic impact and freezing behaviors affect the vapor transfer, we compare the magnitude of three time scales for the mother drop: the spreading time t_s, the cooling time t_c, and the icing nucleation time t_n. First, the spreading time is determined by the drop size and liquid properties, $t_s \sim \mu r / \sigma$, where μ is the dynamic viscosity of water and r is the drop radius before impact. The magnitude of t_s is approximately 10 ms for the given parameter settings [39]. Second, the cooling time t_c can be estimated by applying the energy balance equation, $t_c Q \sim \rho V C_p \Delta T$, where $Q \sim kA\frac{T_\infty - T_{surf}}{h}$ is the average heat transfer rate occurring at the contact area, with V being the drop volume, C_p being the specific heat of water, $\Delta T = T_\infty - T_{surf}$ being the temperature difference of the pendant main drop and the supercooled substrate, k being the thermal conductivity of water, and A being the contact area. Introducing a geometrical factor $f(\theta) = \left(\frac{\sin\theta}{1+\cos\theta}\right)^3 \left(1 - \frac{\sin\theta}{3+3\cos\theta}\right)$ and the thermal diffusivity $\alpha \equiv \frac{k}{\rho C_p}$, with θ being the equilibrium contact angle, we can obtain $t_c \sim r_c^2 f(\theta)/\alpha$, meaning the magnitude of t_c depends on the contact angle and the contact radius [44]. Lastly, the icing nucleation time t_n can be evaluated by adopting Fletcher's classic nucleation theory for heterogeneous icing nucleation and assuming the foreign particle with the size approaching infinity (i.e., a flat surface), $t_n \sim 1/J$ and $J = K\exp(-\Delta G*/k_B T)$ [45,46], with J being the nucleation rate, K being a kinetic constant, $\Delta G*$ being the free energy barrier for heterogeneous icing nucleation, and k_B being the Boltzmann constant. Note that J is determined largely by $\Delta G*$, which in turn strongly depends on the degree of supercooling. We can thus deduce that the magnitude of t_n varies drastically when the substrate temperature changes from $-15.4\,°C$ to $-22.1\,°C$.

After analyzing the three time scales, we can then explain the impact and freezing behaviors of the mother drop. More importantly, we can illustrate how such drop behaviors affect the vapor transfer kinetics and yield the resultant ice coverage, as shown schematically in Figure 7. For a higher substrate temperature at regime I, $t_s < t_c < t_n$, the impinging mother drop goes through a typical spread-recoil process and becomes stabilized. Subsequently, the drop is supercooled to a temperature close to the substrate temperature T_s, and then icing nucleation occurs at the liquid-substrate interface. Both the bright halo and the depletion zone stem from the complete spread-recoil process. The bright halo is caused by overlapping condensation/frosting near the maximum spreading, and the physics were revealed in our earlier work [39]. The depletion zone is caused by the receding contact line, which collects condensate produced in the spreading, leaving the following newly formed condensate microdrops readily evaporated off once the mother drop is frozen. Note that the mother drop is supercooled before icing nucleation occurs; the freezing thus includes a rapid recalescence stage when a large amount of vapor is released [40], explaining why the mother drop in regime I yields a much larger ice coverage. For a lower substrate temperature at regime II, $t_n < t_s < t_c$, spreading of the mother drop is interrupted by icing nucleation, which pins the contact line. In addition, icing nucleation occurs so fast that the remaining liquid inside the mother drop is still warm. Accordingly, the freezing occurs isothermally, and the emission of vapor is suppressed comparing to that of regime I. Note that once the mother drop is frozen completely, vapor emission stops, and thus the condensate/frost region ceases to expand. The total freezing time for regime

II is much shorter than that of regime I due to an apparently larger contact area, which is also one reason why the actual ice coverage for regime II is smaller.
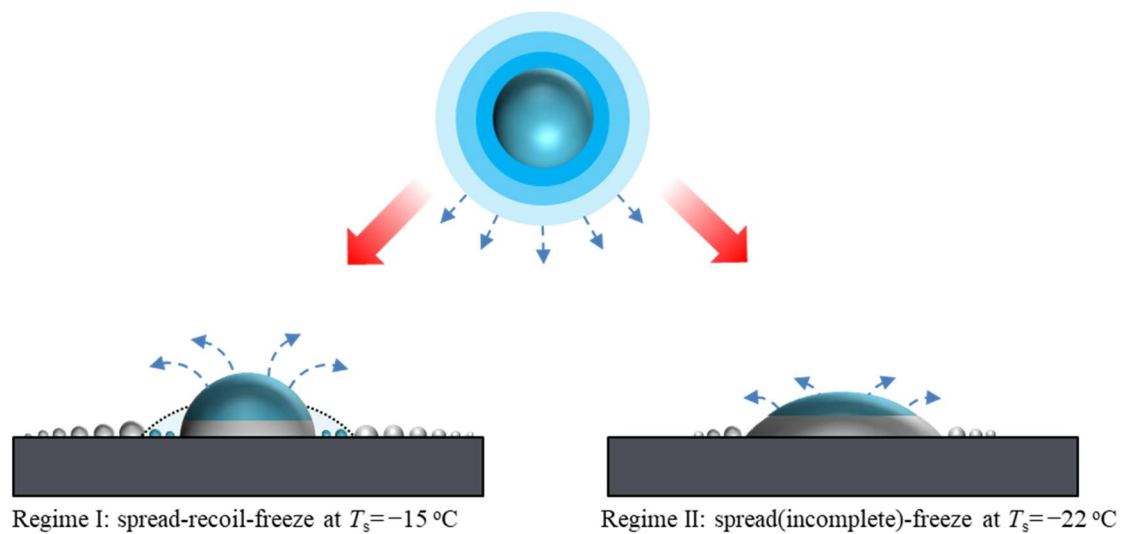
Figure 7. Schematics of the vapor transfer from an impinging drop to the surrounding substrate at two different freezing regimes.

4. Conclusions

In summary, we experimentally studied the freezing of an impinging drop on the supercooled substrate in extremely low vapor pressure, mimicking the scene of aircraft icing. Unlike what has been reported in the literature, we placed our focus on the vapor transfer accompanying the impact and freezing of the impinging drop. We find the actual ice coverage induced by an impinging drop is much larger than the area covered directly by the frozen drop itself. By comparing the two freezing regimes, we show smaller supercooling yields a larger ice coverage due to the extra vapor emission in the recalescence stage and a prolonged freezing time of the impinging drop. The physics revealed in this work can benefit the rational designs of anti-/de-icing technologies that aim to mitigate aircraft icing problems.

References

1. Ahmadi, S.F.; Nath, S.; Kingett, C.M.; Yue, P.; Boreyko, J.B. How soap bubbles freeze. *Nat. Commun.* **2019**, *10*, 2531. [CrossRef]
2. Zhao, Y.; Yang, C.; Cheng, P. Freezing of a nanofluid droplet: From a pointy tip to flat plateau. *Appl. Phys. Lett.* **2021**, *118*, 141602. [CrossRef]

3.   Ma, R.; Cao, D.; Zhu, C.; Tian, Y.; Peng, J.; Guo, J.; Chen, J.; Li, X.-Z.; Francisco, J.S.; Zeng, X.C.; et al. Atomic imaging of the edge structure and growth of a two-dimensional hexagonal ice. *Nature* **2020**, *577*, 60–63. [CrossRef]
4.   Murray, B.J.; Knopf, D.A.; Bertram, A.K. The formation of cubic ice under conditions relevant to Earth's atmosphere. *Nature* **2005**, *434*, 202–205. [CrossRef] [PubMed]
5.   Zhao, Y.; Guo, Q.; Lin, T.; Cheng, P. A review of recent literature on icing phenomena: Transport mechanisms, their modulations and controls. *Int. J. Heat Mass Transf.* **2020**, *159*, 120074. [CrossRef]
6.   John Morris, G.; Acton, E.; Murray, B.J.; Fonseca, F. Freezing injury: The special case of the sperm cell. *Cryobiology* **2012**, *64*, 71–80. [CrossRef] [PubMed]
7.   Song, M.; Dang, C. Review on the measurement and calculation of frost characteristics. *Int. J. Heat Mass Transf.* **2018**, *124*, 586–614. [CrossRef]
8.   Nath, S.; Ahmadi, S.F.; Boreyko, J.B. A Review of Condensation Frosting. *Nanoscale Microscale Thermophys. Eng.* **2017**, *21*, 81–101. [CrossRef]
9.   Zhao, Y.; Zhang, H.; Wang, W.; Yang, C. Wetting transition of sessile and condensate droplets on copper-based superhydrophobic surfaces. *Int. J. Heat Mass Transf.* **2018**, *127*, 280–288. [CrossRef]
10. Haque, M.R.; Das, S.R.; Betz, A.R. Experimental investigation of condensation and freezing phenomena on hydrophilic and hydrophobic graphene coating. *Appl. Therm. Eng.* **2019**, *160*, 113987. [CrossRef]
11. Zhao, Y.; Yang, C. Frost spreading on microscale wettability/morphology patterned surfaces. *Appl. Therm. Eng.* **2017**, *121*, 136–145. [CrossRef]
12. Zhao, Y.; Yang, C. Retarded condensate freezing propagation on superhydrophobic surfaces patterned with micropillars. *Appl. Phys. Lett.* **2016**, *108*, 061605. [CrossRef]
13. Yao, Y.; Zhao, T.Y.; Machado, C.; Feldman, E.; Patankar, N.A.; Park, K.-C. Frost-free zone on macrotextured surfaces. *Proc. Natl. Acad. Sci. USA* **2020**, *117*, 6323. [CrossRef]
14. Mitridis, E.; Schutzius, T.M.; Sicher, A.; Hail, C.U.; Eghlidi, H.; Poulikakos, D. Metasurfaces Leveraging Solar Energy for Icephobicity. *ACS Nano* **2018**, *12*, 7009–7017. [CrossRef]
15. Zhao, Y.; Yan, Z.; Zhang, H.; Yang, C.; Cheng, P. Promote anti- /de- frosting by suppressing directional ice bridging. *Int. J. Heat Mass Transf.* **2021**, *165*, 120609. [CrossRef]
16. Gurumukhi, Y.; Chavan, S.; Sett, S.; Boyina, K.; Ramesh, S.; Sokalski, P.; Fortelka, K.; Lira, M.; Park, D.; Chen, J.-Y.; et al. Dynamic Defrosting on Superhydrophobic and Biphilic Surfaces. *Matter* **2020**. [CrossRef]
17. De Koninck, L.H.; Ahmadi, S.F.; Boreyko, J.B. Passive anti-frosting cables. *Int. J. Heat Mass Transf.* **2020**, *146*, 118808. [CrossRef]
18. Ahmadi, S.F.; Spohn, C.A.; Nath, S.; Boreyko, J.B. Suppressing Condensation Frosting Using an Out-of-Plane Dry Zone. *Langmuir* **2020**, *36*, 15603–15609. [CrossRef] [PubMed]
19. Cebeci, T.; Kafyeke, F. Aircraft Icing. *Annu. Rev. Fluid Mech.* **2003**, *35*, 11–21. [CrossRef]
20. Fernandez-Gonzalez, S.; Sanchez, J.L.; Gascon, E.; Lopez, L.; Garcia-Ortega, E.; Merino, A. Weather Features Associated with Aircraft Icing Conditions: A Case Study. *Sci. World J.* **2014**, *2014*, 18. [CrossRef] [PubMed]
21. Schutzius, T.M.; Jung, S.; Maitra, T.; Graeber, G.; Köhme, M.; Poulikakos, D. Spontaneous droplet trampolining on rigid superhydrophobic surfaces. *Nature* **2015**, *527*, 82–85. [CrossRef]
22. Kant, P.; Koldeweij, R.B.J.; Harth, K.; van Limbeek, M.A.J.; Lohse, D. Fast-freezing kinetics inside a droplet impacting on a cold surface. *Proc. Natl. Acad. Sci. USA* **2020**, *117*, 2788. [CrossRef]
23. Josserand, C.; Thoroddsen, S.T. Drop Impact on a Solid Surface. *Annu. Rev. Fluid Mech.* **2016**, *48*, 365–391. [CrossRef]
24. Wang, Y.; Ju, L.; Han, D.; Wang, Q. Numerical investigation of the impacting and freezing process of a single supercooled water droplet. *Phys. Fluids* **2021**, *33*, 042114. [CrossRef]
25. Graeber, G.; Schutzius, T.M.; Eghlidi, H.; Poulikakos, D. Spontaneous self-dislodging of freezing water droplets and the role of wettability. *Proc. Natl. Acad. Sci. USA* **2017**, *114*, 11040–11045. [CrossRef] [PubMed]
26. Jung, S.; Tiwari, M.K.; Doan, N.V.; Poulikakos, D. Mechanism of supercooled droplet freezing on surfaces. *Nat. Commun.* **2012**, *3*, 615. [CrossRef] [PubMed]
27. Kim, H.; Lee, C.; Kim, M.H.; Kim, J. Drop Impact Characteristics and Structure Effects of Hydrophobic Surfaces with Micro- and/or Nanoscaled Structures. *Langmuir* **2012**, *28*, 11250–11257. [CrossRef]
28. Meuler, A.J.; McKinley, G.H.; Cohen, R.E. Exploiting Topographical Texture To Impart Icephobicity. *ACS Nano* **2010**, *4*, 7048–7052. [CrossRef] [PubMed]
29. Mishchenko, L.; Hatton, B.; Bahadur, V.; Taylor, J.A.; Krupenkin, T.; Aizenberg, J. Design of Ice-free Nanostructured Surfaces Based on Repulsion of Impacting Water Droplets. *ACS Nano* **2010**, *4*, 7699–7707. [CrossRef]
30. Ma, Z.; Xiong, W.; Cheng, P. 3D Lattice Boltzmann simulations for water droplet's impact and transition from central-pointy icing pattern to central-concave icing pattern on supercooled surfaces. Part II: Rough surfaces. *Int. J. Heat Mass Transf.* **2021**, *172*, 121153. [CrossRef]
31. Marín, A.G.; Enríquez, O.R.; Brunet, P.; Colinet, P.; Snoeijer, J.H. Universality of Tip Singularity Formation in Freezing Water Drops. *Phys. Rev. Lett.* **2014**, *113*, 054301. [CrossRef]
32. Shang, Y.; Liu, X.; Bai, B.; Zhong, X. Central-pointy to central-concave icing transition of an impact droplet by increasing surface subcooling. *Int. Commun. Heat Mass Transf.* **2019**, *108*, 104326. [CrossRef]

33. Yao, Y.; Li, C.; Zhang, H.; Yang, R. Modelling the impact, spreading and freezing of a water droplet on horizontal and inclined superhydrophobic cooled surfaces. *Appl. Surf. Sci.* **2017**, *419*, 52–62. [CrossRef]

34. Xiong, W.; Cheng, P. Numerical investigation of air entrapment in a molten droplet impacting and solidifying on a cold smooth substrate by 3D lattice Boltzmann method. *Int. J. Heat Mass Transf.* **2018**, *124*, 1262–1274. [CrossRef]

35. Zhang, H.; Zhao, Y.; Fang, W.; Zhang, C.; Zhu, F.; Jin, L.; Yang, C. Active control of the freezing process of a ferrofluid droplet with magnetic fields. *Appl. Therm. Eng.* **2020**, *176*, 115444. [CrossRef]

36. Kant, P.; Müller-Groeling, H.; Lohse, D. Pattern Formation during the Impact of a Partially Frozen Binary Droplet on a Cold Surface. *Phys. Rev. Lett.* **2020**, *125*, 184501. [CrossRef]

37. Bai, G.; Gao, D.; Liu, Z.; Zhou, X.; Wang, J. Probing the critical nucleus size for ice formation with graphene oxide nanosheets. *Nature* **2019**, *576*, 437–441. [CrossRef] [PubMed]

38. Chu, F.; Zhang, X.; Li, S.; Jin, H.; Zhang, J.; Wu, X.; Wen, D. Bubble formation in freezing droplets. *Phys. Rev. Fluids* **2019**, *4*, 071601. [CrossRef]

39. Zhao, Y.; Zhu, F.; Zhang, H.; New, T.H.; Jin, L.; Yang, C. Triple condensate halo from a single water droplet impacting upon a cold surface. *Appl. Phys. Lett.* **2019**, *114*, 183703. [CrossRef]

40. Jung, S.; Tiwari, M.K.; Poulikakos, D. Frost halos from supercooled water droplets. *Proc. Natl. Acad. Sci. USA* **2012**, *109*, 16073–16078. [CrossRef] [PubMed]

41. Miljkovic, N.; Preston, D.J.; Enright, R.; Wang, E.N. Electric-Field-Enhanced Condensation on Superhydrophobic Nanostructured Surfaces. *ACS Nano* **2013**. [CrossRef] [PubMed]

42. Zhao, Y.; Lin, R.; Tran, T.; Yang, C. Confined wetting of water on CNT web patterned surfaces. *Appl. Phys. Lett.* **2017**, *111*, 161604. [CrossRef]

43. Clanet, C.; Beguin, C.; Richard, D.; Quere, D. Maximal deformation of an impacting drop. *J. Fluid Mech.* **2004**, *517*, 199–208. [CrossRef]

44. Xiong, W.; Cheng, P. Mesoscale simulation of a molten droplet impacting and solidifying on a cold rough substrate. *Int. Commun. Heat Mass Transf.* **2018**, *98*, 248–257. [CrossRef]

45. Fletcher, N.H. *The Chemical Physics of Ice*; Cambridge University Press: Cambridge, UK, 1970. [CrossRef]

46. Fletcher, N.H. Size Effect in Heterogeneous Nucleation. *J. Chem. Phys.* **1958**, *29*, 572–576. [CrossRef]